Optical elastography: tracking surface waves with digital image correlation

Ali Zorgani, Tarek Abdul Ghafour, Maxime Lescanne, Stefan Catheline, Aline Bel-Brunon

Physics in Medicine & Biology

PAPER

Optical elastography: tracking surface waves with digital image correlation

To cite this article: Ali Zorgani *et al* 2019 *Phys. Med. Biol.* **64** 055007

IOP Publishing Phys. Med. Biol. 64 (2019) 055007 (9pp) https://doi.org/10.1088/1361-6560/ab0141

Physics in Medicine & Biology

IPEM Institute of Physics and Engineering in Medicine

PAPER

Optical elastography: tracking surface waves with digital image correlation

RECEIVED
25 October 2018

REVISED
16 January 2019

ACCEPTED FOR PUBLICATION
23 January 2019

PUBLISHED
25 February 2019

Ali Zorgani[1,3], Tarek Abdul Ghafour[2], Maxime Lescanne[1], Stefan Catheline[1] and Aline Bel-Brunon[2]

[1] LabTAU, INSERM, Centre Léon Bérard, Université Lyon 1, Univ Lyon, F-69003, LYON, France
[2] Univ Lyon, INSA-Lyon, CNRS UMR5259, LaMCoS, F-69621, France
[3] Author to whom any correspondence should be addressed.

E-mail: ali.zorgani@inserm.fr

Keywords: surface waves, wave speed, optics, correlation, elastography, time of flight

Abstract

Elastography consists in evaluating the propagation speed of waves into a tissue to estimate its stiffness. Usually this method is based on Ultrasounds, magnetic resonance imaging or optical coherent tomography. This paper proposes a simple optic method using ultrafast cameras. Based on digital image correlation (DIC), the tracking of elastic surface wave from white light intensity pattern, allows estimating the propagation speed as an indicator of the tissue local stiffness. Two configurations are presented: (1) 2D imaging of a flat phantom surface with a single camera and (2) 3D imaging of a curved phantom surface with two cameras. As a feasibility study of the first configuration, surface wave speed was measured on isotropic and anisotropic phantoms. Comparisons with ultrasound methods fully validate this approach. Although more sophisticated, the second configuration account for propagation distortions caused by locally curved topology. Triangulation techniques used to retrieve local topology are named stereo-correlation in the field of biomechanics. Stereo-elastography is thus proposed to determine tissue local elasticity from any soft tissue surface wave.

1. Introduction

Ultrasound shear wave elastography is a well-developed modality for mapping soft tissue elasticity in clinics. It consists in imaging the propagation of an actively (internally or externally) induced shear wave. Under the assumption of homogeneous elastic tissue, the shear modulus μ is proportional to the shear wave speed C_s according to the relationship $\mu = \rho C_s^2$, where ρ is the tissue density (Royer and Dieulesaint 2000). Two kind of shear wave sources are used, external mechanical vibrator (Catheline *et al* 1999, Sandrin *et al* 2003) and radiation pressure (Sugimoto *et al* 1990, Nightingale *et al* 2002, Bercoff *et al* 2004). Several imaging modalities can be used to image the resulting displacement: Ultrasound (Sandrin *et al* 1999), magnetic resonance elastography (MRE) (Sarvazyan *et al* 1998), optical coherence tomography (OCT) (Wang and Larin 2014). These methods allow observing the shear wave propagation inside a tissue to evaluate its speed and therefore, determine its elasticity.

On the one hand, it has been reported with laser or acoustic methods, that the relationship between the shear wave speed and the shear modulus is also valid for surface waves (Zhang and Greenleaf 2007). A few papers propose methods that use this principle to evaluate tissue elasticity using digital holography (Li *et al* 2011, Liu *et al* 2017) or full-field optical coherence (Nahas *et al* 2013). These methods can reach high frequencies, sufficient to catch a wave propagating on a soft medium, and have also demonstrated the potentiality to detect subsurface phenomena such as multilayers or inclusions. However, they are restricted to small area of interest and plane surfaces.

On the other hand, deformations on solid surface can be measured using digital image correlation (DIC) (Sutton *et al* 2009). This method consists in comparing images of a solid surface in undeformed (reference) and deformed states, the observed surface being covered with a random pattern (naturally present (Bel-Brunon *et al* 2014) or applied using paint or make-up (Jacquemoud *et al* 2007, Brunon *et al* 2010)). Using a correlation algorithm, one can determine the displacement field on the solid surface. If the surface is plane, images are acquired

with one camera and DIC is 2D. If it is non-plane, images are acquired with two cameras forming an angle to perform stereovision; using images from the two cameras, stereo-correlation provides the non-plane surface and the displacement field on this surface. Both methods have been widely used in the field of solid mechanics, particularly in soft tissue mechanics as they allow accurate measurement of boundary conditions, see for instance (Boyce *et al* 2008, Moerman *et al* 2009, Gao and Desai 2010), or to study local phenomena such as rupture.

The aim of the present work is to evaluate whether DIC technics could detect and evaluate the speed of elastic waves propagating on a soft solid, to be further used for elastography purposes. The main improvement of the proposed method compared to the existing ones is to handle large areas of interest with rather large curvatures, with a single measurement. In order to answer this question, an experimental set-up was built to test two configurations. First, feasibility experiments to visualize small vibrations due to surface wave propagation on a plane isotropic phantom and a plane transversely isotropic phantom are presented. Second, 3D imaging of surface wave propagation was performed on a dome-like shaped gelatin phantom. This paper consists in a feasibility study for the evaluation of the surface wave speed in the three described cases. Section 2 is focused on the phantom elaboration and experimental set-up description. Section 3 presents the speed evaluation results with an estimation of the method accuracy. In section 4, we discuss our method and results, before concluding in section 5.

2. Material and methods

2.1. Tissue mimicking phantoms preparation

2.1.1. Isotropic phantoms

The first experiment was conducted on a homemade isotropic tissue-mimicking phantom. It contains 5% (w/v) of gelatin (Sigma Aldrich, St Louis, MO, USA) for stiffness control and 0.5% (w/v) of graphite (Sigma Aldrich, St Louis, MO, USA) in order to create optical speckle on the surface of the phantom. The solution was poured into a rectangular mold (20 × 10 × 4 cm) and kept into the fridge during 1 h at 4 °C for cooling. The obtained phantom had therefore a plane upper surface.

The same method was used to make the dome-like phantom required for the 3D experiments. The solution was poured into a bowl (10 cm diameter) to obtain a dome-like shape. Due to gravity, the dome was not completely spherical once put on the testing table; the real shape could however be caught by stero-correlation (see section 2.2.2).

2.1.2. Anisotropic phantom

A transversely isotropic tissue-mimicking phantom was made of a polyvinyl alcohol (PVA) solution (Chatelin *et al* 2014). The phantom was prepared from a solution of 5% (w/v) of PVA (molecular weight 89 000–98 000, 99+% hydrolyzed, Sigma-Aldrich, St Louis, US) diluted in degassed water at 90 °C. Then, 0.5% (w/v) of graphite (Sigma Aldrich, St Louis, MO, USA) has been added to the PVA solution to create an optical speckle at the phantom surface. The solution was poured into a mold (20 × 10 × 4 cm) and underwent two freeze/thaw cycles i.e. −18 °C during 12 h and 20 °C during 12 h. Then, the sample was stretched to about 180% of its initial length as illustrated by Chatelin *et al* (2014), and underwent three more freeze/thaw cycles. In the following, axis Y is the longitudinal direction, i.e. the direction that over went an elongation. The sample was finally placed in the fridge at 4 °C to freeze.

2.1.3. Random speckle pattern for digital image correlation

Digital image correlation algorithm needs a stationary random pattern of intensity light on the tissue surface. In some cases, the tissue natural pattern is sufficient; this was the case for our two plane phantoms (isotropic and anisotropic) thanks to the graphite particles. However, due to a higher field-of-view and therefore, to a lower spatial resolution, this was insufficient for the dome-like phantom. Therefore, a white paint spray was used in order to create a speckle pattern on top of the phantom surface. Paint drops dried almost instantaneously, allowing the test to be performed shortly after its application, so as to prevent the phantom from exceeding the room temperature due to light spots, which will affect the speed measurement.

2.2. Experimental set-up

2.2.1. 2D experiments

An ultrafast digital camera (Phantom® v710) equipped with a ×2 telecentric lens was positioned vertically above the phantom (figure 1), and connected to a host computer for digital images storing. The telecentric lens is used to prevent computing artificial dilatation due to potential out-of-plane displacements: telecentric lens indeed receives light rays in a single direction, perpendicular to the camera sensor. Therefore an area of the observed solid that experiences out-of-plane displacement does not appear larger or smaller on the camera lens than its initial position. Thus using a telecentric lens allows to remove out-of-plane displacements from the

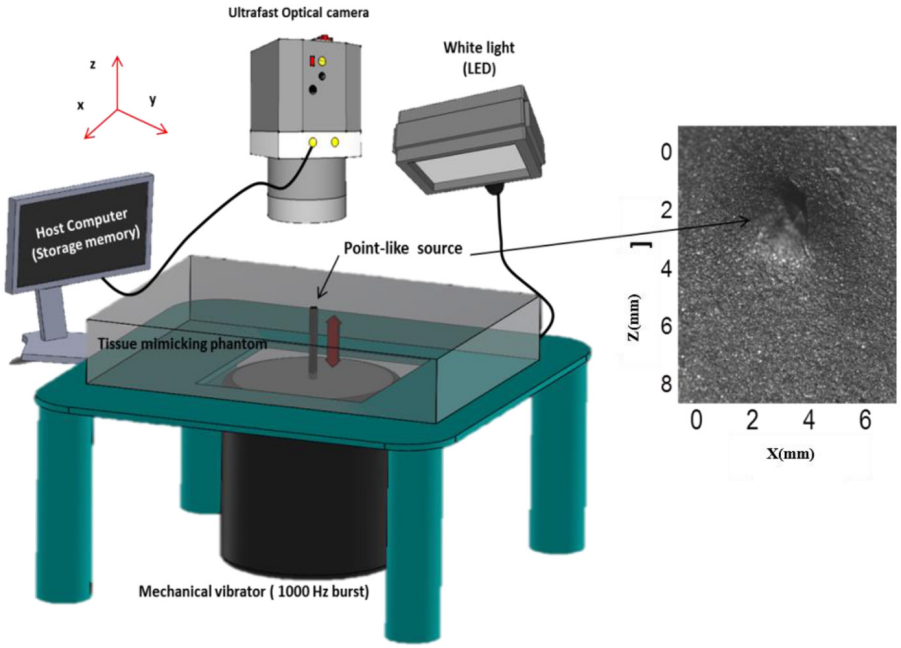

Figure 1. Description of the plane surface experimental set-up. The phantom surface was imaged using an ultrafast optical camera located on top. Elastic surface waves are generated by a rigid rod mounted on a vibrator; the rod is inserted within the phantom from the bottom surface until just below the upper surface. In a post-processing step, surface wave detection is performed using digital image correlation. A typical snapshot is presented on the right hand side.

acquired; if the obtained computed strain field includes dilatation or shrinkage, one can be sure that it comes from actual dilatation or shrinkage of the solid and not from out-of-plane displacements (Jones 2018). This implies that the field of view is limited by the camera sensor size. In the proposed set-up, the camera sensor size was 1280 × 800 px^2 corresponding to 25 × 16 mm^2; the corresponding field of view on the sample was 12.5 × 8 mm^2. The frame rate was set to 4000 frames s^{-1}. The phantom surface was illuminated by a powerful white light (LED) to obtain a good contrast even with a small image exposure time. A cylindrical source (1 mm diameter metal rod) was mounted on a mechanical vibrator (figure 1) and excited by a 1000 Hz impulse in order to induce surface wave. To prevent the source from being present in the imaging field, it was inserted in the bulk of the phantom until it reached the surface (figure 1 (right)). The generator was synchronized with the ultrafast camera in order to trigger the acquisition.

2.2.2. 3D experiments

Elastography is usually applied to soft organs *in vivo*; therefore the external surface of the imaged object is never plane. As mentioned above, for this kind of surfaces a stereo-vision system is needed in order to perform an accurate measurement of the wave speed, independent of topologic distortion induced by curved surface.

To mimic the case of surface wave propagation on a curved surface, the experiment was conducted on the homemade dome-like gelatin phantom (figure 2(b)). A stereo-vision system composed of two synchronized ultra-fast cameras (Photron® FastCam SA3) equipped with two 60 mm lens, was placed above the sample so as to form an angle of 15 to 30° with each other (preconized angle range to ensure the digital image correlation algorithm convergence). The exact relative position of the two cameras is computed by the digital image correlation software (Vic® 3D) from calibration images acquired using a calibration object provided by Vic® 3D (white plate with 12 black dots distributed on 4 lines and 3 rows, distant of 3 mm from each other) (Sutton *et al* 2009). Each camera had a resolution of 1024 × 1052 px^2. Their position was secured using a rigid fixing system mounted on a dedicated aluminum bar structure. The same set-up parameters (loading, acquisition frequency) as in the 2D experiment were used.

2.3. Displacement field computation by digital image correlation

The induced displacement field were computed by digital image correlation with the software Vic® 3D from the 100 first images saved in the memory of the host computer. This technique calculates the displacement field between an undeformed (reference) configuration and a deformed configuration (Sutton *et al* 2009). Vic® 3D provides the two in-plane components (U and V) of the displacement field parallel to the surface, and in the case of stereo-correlation, the out-of-plane component (W) of the displacement.

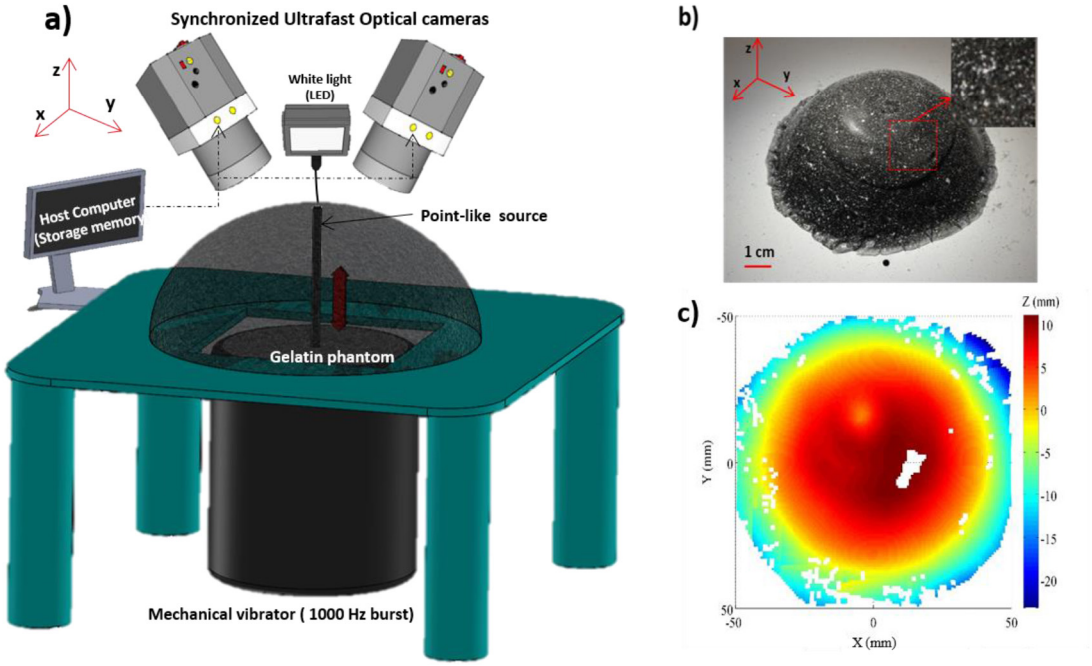

Figure 2. (a) Experimental setup of stero-elastography. In order to reconstruct the topology of a non-plane surface on the base of triangulation, two ultrafast camera performs stereo-correlation. Elastic surface waves are generated by a rigid rod mounted on a vibrator. (b) A picture of the dome-like gelatin phantom is presented with a zoom of the speckle pattern on the top-right panel. (c) Altitude of the phantom surface reconstructed using stereo-correlation.

3. Results

3.1. DIC quality

3.1.1. 2D experiment

To compute the displacement field at the sample surface, the software divides the user-defined area of interest into subsets which size and step (shift from one subset to the other) are adjusted; if step is smaller than size, then neighboring subsets have a shared area. The subset size has to be consistent with the random pattern. Indeed, the higher is the size, the smoother will be the obtained field; the higher is the step, the coarser will be the obtained field. A typical value is 21 pixels for the subset and 7 pixels for the step.

A way to evaluate the DIC quality is to compute the displacement field between several images of the same state, for instance the reference state. The obtained variability on the displacement is due to sensor noise, light variations, low quality of the pattern, inappropriate subset size, etc. It depends on the optical set-up, the speckle pattern and the DIC algorithm.

Figure 3 displays the distribution of the variability over the area of interest and the evolution of the maximal variability with subset size for the 2D-correlation set-up. The maximal variability is located at the top of the point-like source because of light reflections, and converges when the subset size increases. Indeed, the gray level distribution information contained in each subset being richer, the algorithm converges more easily to the new configuration of each subset.

The maximal variability for a subset of 0.79 mm (79 px) is roughly 10^{-4} mm for our optical set-up for in-plane displacements. Once the point-like source is excited and the wave propagates, the worst case corresponds to a maximal variability of 0.04 px, i.e. $4 \cdot 10^{-4}$ mm. However, it has the same distribution as for the noise variability, so most of the area of interest is actually computed with a much smaller variability; during the wave propagation, the variability in the blue area (figure 3(a)) is below $8 \cdot 10^{-5}$ mm. As a comparison typical wave amplitude is 0.1 mm so the relative variability around 10^{-3} validates the detection approach.

3.1.2. 3D experiment

In stereo-correlation, the image processing is performed in the area seen by both cameras. In the presented set-up, a large part of the dome could be included in the stereo-correlation computation (figure 2(c)). For quality computation, the area of interest was a circle of 67 mm (609 px) of diameter (figure 4(a)). The calibration was performed from 13 sets of images of the calibration object. The overall score was 0.026 px ($2.9 \cdot 10^{-3}$ mm), corresponding to the average error between the position where a target point of the calibration object was found in the image, and the theoretical position where the mathematical calibration model places the point. The calibration also indicated that the two cameras had a relative angle of 19.256°, which falls in the recommended

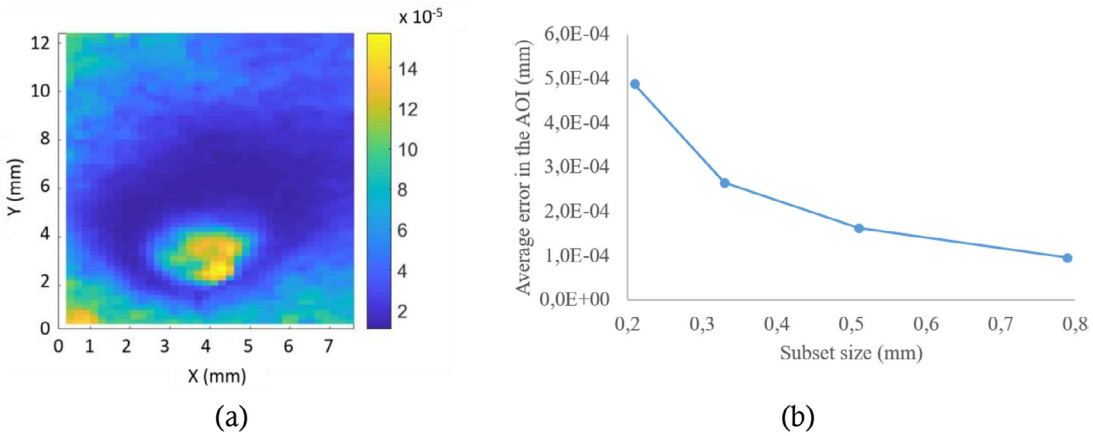

Figure 3. Variability measurement in the 2D experiment. (a) As expected, the color map variability distribution (in mm) over the area of interest (subset size 51 px) shows a maximum in the source region; (b) the average variability value is represented versus the subset size. Compared with typical wave amplitude (0.1 mm), this variability is not an obstacle for detection.

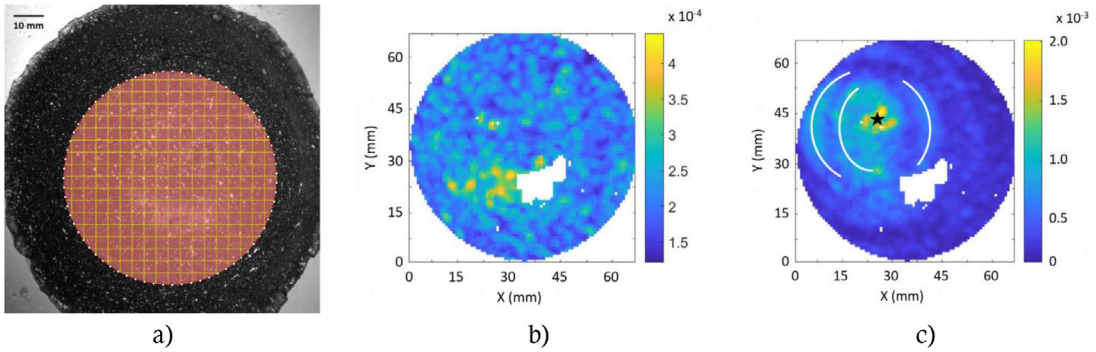

Figure 4. Error distribution obtained by stereo-correlation (in mm): (a) area of interest (AOI) plotted over a view of the sample; (b) error distribution due to measurement noise over the curved surface of the dome, (c) error distribution after the wave propagation has started (white lines: wave fronts; black star: point-like source). Here the step is 12 px (1.2 mm).

range for stereo-DIC. The variability distribution on the curved surface is displayed on figures 4(b) and (c) for a subset size of 37 px corresponding to 4.07 mm. We can see a hole corresponding to an over-exposed area, where stereo-DIC cannot be performed. The maximal variability due to noise in the area of interest is $4.5 \cdot 10^{-4}$ mm.

Once the point-like source is excited, the maximal variability occurs just around it (figure 4(c)). It reaches $1.8 \cdot 10^{-3}$ mm. However, it is much localized; in the area of propagation (AOI except point-like source and over-exposed area), it remains below 10^{-3} mm for all images. As we wanted to test the algorithm and set-up capacities, a typical wave amplitude in elastography of ± 0.05 mm was selected, so the displacement description is accurate within 20%. This uncertainty is acceptable and allows a good speed estimation as shown in the last part of the manuscript.

3.2. Wave speed measurement for the 2D experiments

3.2.1. Digital image correlation measurements for the isotropic gel

An estimation of the out-of-plane component dW/dz is computed from the two other components of the displacement field using:

$$\frac{dW}{dz} = -\left(\frac{dU}{dx} + \frac{dV}{dy}\right).$$

The choice of observable, the out-of-plane gradient, results from the divergence free nature of the displacement field in an incompressible soft solid. It simplifies the representation of the vectorial elastic field into a scalar field that have a great advantage to present an omnidirectional directivity pattern for the source. Thereby, time of flight techniques used to estimate speed could be computed in all directions.

The resulting dimensionless scalar field for the isotropic phantom is presented on six snapshots (figure 5(a)). The induced displacements are clearly visible as a cylindrical wave front propagating from the position of the point source toward the boundaries. The amplitude of this displacement is ranging between ± 0.5 mm. The speed of the surface wave can be measured from the seismic-like representation (figure 5(b)). The slopes (red

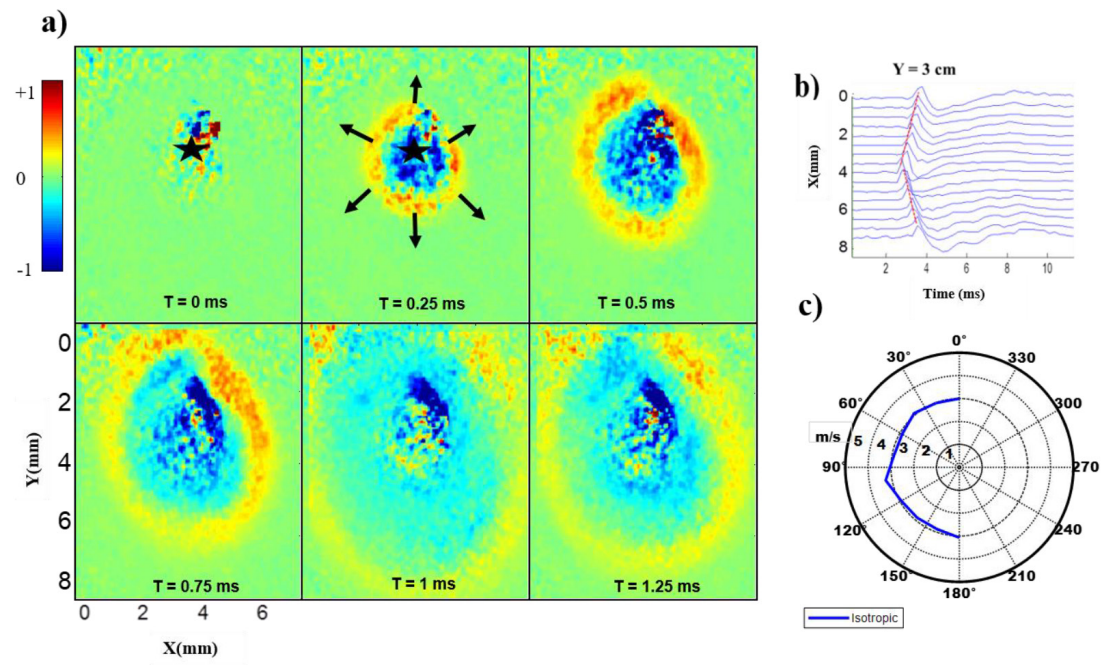

Figure 5. Surface wave propagation on the isotropic phantom: (a) six snaphots represents the out-of-plane gradient component $\frac{dW}{dz}$ of the induced wave front. The monopole nature of the pulse source is clearly apparent. (b) From a seismic-like representation of the field, the wave propagation in the Y direction gives a speed estimation $C_{surface} = 2.53 \pm 0.32$ m s^{-1}. (c) Plotted in polar coordinate the wave speed measurement confirms as expected the isotropy of the phantom.

dotted lines) are representative of the wave speed in the x direction on both sides of the source. Measurements in radial directions are performed and give an average a value of 2.35 ± 0.3 m s^{-1}. This value is in good agreement with ultrasound transient elastography measurements (Bercoff *et al* 2004) and confirm the similarity between surface wave and bulk shear waves ($C_{surface} = 0.96\, C_{shear}$, (Royer and Dieulesaint 2000)). Note that these surface waves could be Rayleigh -like waves, with the caveat that the air is not a perfect vacuum. Besides, a relative error of 12% is similar to the typical error of elastography due to displacement estimation from ultrasound speckle (Walker and Trahey 1994). Monopole nature of the source is clearly visible in these first experimental results represented in polar coordinates (figure 5(c)) which confirms as expected, the isotropy of the phantom.

3.2.2. Digital image correlation measurements for the transversely isotropic gel

The ability of this approach to capture the anisotropy of a simple soft solid—a PVA phantom—using surface wave measurements is now investigated. Figure 6(a) displays the six first snapshots of the amplitude of the displacement field. The ellipse-like shape of the wave front is apparent when compared to the circular shape obtained with the isotropic phantom; it is even more obvious on the polar coordinate representation (figure 6(d)). The wave speed in the transversal direction X (figure 6(b)) $C_{surface\_x} = 3.08 \pm 0.24$ m s^{-1} is compared to the surface wave computed in the longitudinal direction Y (figure 6(b)) $C_{surface\_y} = 4.02 \pm 0.48$ m s^{-1}. As expected, the wave propagates faster in the direction of stretching. The speed ratio between directions Y and X (23%) is therefore comparable to what was obtained in Chatelin *et al* (2014).

3.3. Wave speed measurements for the 3D experiment

Now that we have shown that surface waves can be detected by DIC on plane samples, we aim to evaluate the possibility to do the same on curved surfaces, much more frequent in *in vivo* applications. Such as, corneas stiffness measurement for glaucoma diagnostic or even skin stiffness measurement at a big scale. Stereo-DIC provides a displacement field in the three directions (2 in plane and 1 out-of-plane) from which the wave speed can be computed.

The dome surface is reconstructed from the combination of images obtained from each camera at several deformation states (see figure 2(c)). Then the software allows to track the wave propagation on the sample curved surface, and to perform an accurate measurement of the surface wave speed. U and V are the in-plane displacements measured parallel to the surface; the stereo-vision system also allows measuring the out-of-plane component of the displacement field W. Figure 7 displays the U, V and W components evolution over time. In our case, the two first components (U and V) are sufficient to measure the surface wave speed. However, the out-of-plane component shows a perfectly spherical wave front. As pointed out in the previous section, this component reveals a mono-polar field in contrast to dipolar field for the in-plane components. It eases the speed estimation in any

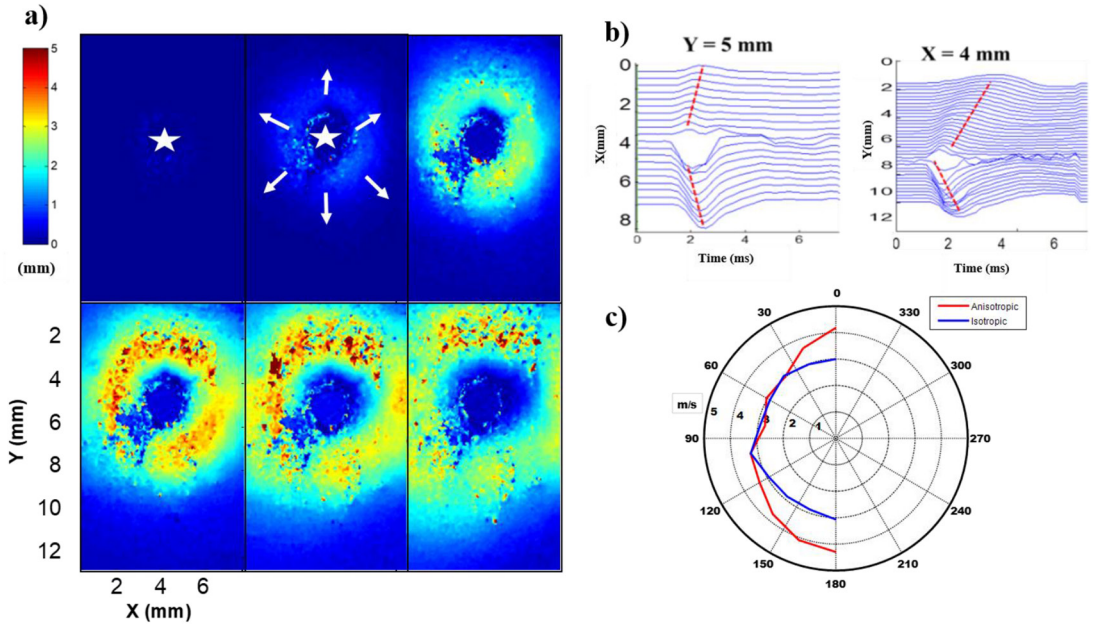

Figure 6. Surface wave propagation on the anisotropic phantom: (a) six snaphots represents the out-of-plane gradient component $\frac{dW}{dz}$ of the induced wave front. (b) From a seismic-like representation of the field, the wave propagation in the x and y directions gives a speed estimation $C_{\text{surface\_y}} = 4.02 \pm 0.48$ m s^{-1} and $C_{\text{surface\_x}} = 3.08 \pm 0.24$ m s^{-1}. (c) Plotted in polar coordinates, the wave speed measurement confirms (red line) as expected the transverse isotropy of the phantom. For comparison, the isotropic estimations are also represented (blue line).

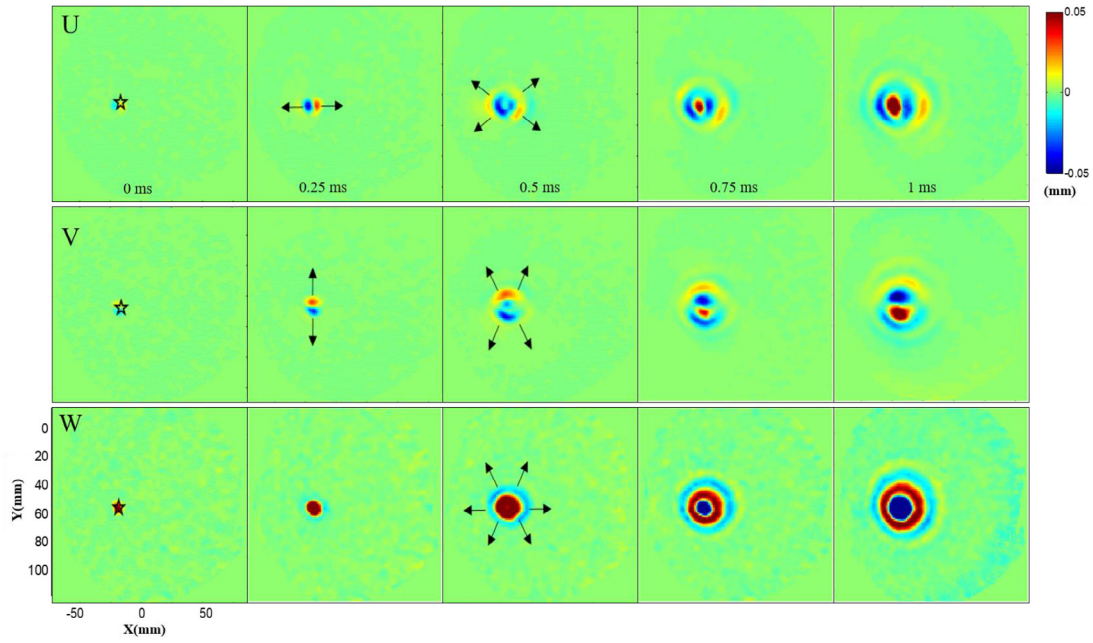

Figure 7. Displacement fields over the dome-like phantom: snapshots of the transversal component U (top) the longitudinal component V (middle) and the out-of-plane component W (bottom). The amplitude of the displacement is ranging between ± 0.05 mm.

direction. The shear wave speed is 2.27 ± 0.24 m s^{-1}. This is in the same order of magnitude as what is usually measured in this kind of tissue-mimicking phantoms and in good agreement with the estimated values on the isotropic plane phantom (same material) (see section 3.2.1).

4. Discussion

In this work, we have investigated the potentiality to use digital image correlation to track surface waves on soft tissues, using ultrafast cameras. This method could be used, under some assumptions on the solid constitution, to investigate soft tissue mechanical properties or at least, to evaluate stiffness heterogeneities or anisotropy in a

solid. It has been shown that surface waves contain information about underlying constituents (inclusion, multi-layers) and could therefore be used as a material identification tool (Li *et al* 2011). The present paper describes both plane and non-plane surface cases; however, it is clear that non-plane case is the most general as it allows describing wave propagation on a much larger area of interest (not limited to camera sensor size) without the constraint of perfectly flat surface. It opens a large field of potential *in vivo* applications, from cell (Grasland-Mongrain *et al* 2018) to tissue characterization (in particular skin, anywhere on the body). The proposed method requires a mechanical solicitation, which can be done by an air puff, a vibrator or even a flick.

In this paper, the source amplitude was chosen to create a large enough surface wave to allow DIC computation. The observed in-plane displacements were between 0.05 and 0.5 mm. For the plane case, the maximal error due to noise is $4 \cdot 10^{-4}$ mm, but does not exceed $8 \cdot 10^{-4}$ mm in the area of measure (where the wave propagates). These results are highly acceptable since (1) the latter amplitudes are in the range of the shear wave amplitudes routinely used in clinics (between 50 and 200 μm) (Catheline *et al* 1999, Sandrin *et al* 2002, 2003) and (2) the estimated noise does not prevent an accurate estimation of speed within the 10% relative error widely accepted in the community of elastography (Athanasiou *et al* 2010, Sporea *et al* 2013). We can point out here the importance of using a telecentric lens, so that the speed measurements are not altered by the out-of-plane displacements. This demonstrates that the 2D measurement accuracy is sufficiently good for a small scale phenomenon like wave propagation. We recommend this method when the area of interest remains reasonably flat since stereovision is more difficult to set up.

As far as stereo-elastography of curved surface is concerned, the precision slightly degrades. The displacements are estimated with a relative uncertainty of about 20%. This seems large, however it should be noticed that the dome curvature is rather high because the area of interest is rather large, leading to a large depth of field, which compromises the displacement accuracy. There is still room for optimizing the optical system and decreasing the error. This is one of the key points of stereo-correlation: choosing the appropriate optical system that provides the appropriate depth of field and field of view. The combination of these two parameters often leads to a compromise that affects the resulting displacement accuracy. As the wave speed calculation is based on the out-of-plane displacement field, one improvement could be to increase the angle between the two cameras: it increases the accuracy on the out-of-plane displacement and decreases the accuracy of the in-plane displacements.

Compared to conventional optical coherent tomography (OCT) or other point-by-point laser methods, the main advantage of DIC is its speed. A single measurement movie, caught in a few millisecond allows reconstructing the elasticity on the entire surface covered by the image. It should be noted though that full-field OCT can compete with this ultrafast frame rate. Except for stereo-vision, DIC is easy to implement, conceptually simpler than interferometers and offers reasonable price. Except for the very high speed cameras (maximum frames per second: 500 000) used in our experiments (~120 k€) our latest acquisition (maximum frames per second: 10 000) is 4 k€ only. When a pulsed surface wave is replaced by a diffuse surface wave, camera with any frame rate can be used to construct a wavelength imaging closely related to tissue stiffness (Zorgani *et al* 2015).

Another advantage of DIC is its adaptability to different samples and different scales. As long as the stereo-vision system has been previously calibrated and firmly mounted, it can be re-used several times. Plane or non-plane samples could also be imaged with the same stereovision system; this would allow a larger field of view for plane samples, and avoid using a telecentric lens. The other advantage is that one can use standard lightening; it should be quite powerful but is easier to set than OCT.

Some drawbacks briefly sketched in previous paragraphs should however be clearly pointed out here. First of all, in contrast with OCT, DIC can only detect surface wave except in transparent media. Second, the need for a random pattern of intensity speckle can also be a disadvantage, as a natural pattern is not always sufficient. Depending on the scale of the observed phenomenon, applying a random pattern can be difficult. However, we have demonstrated here that a very simple method (paint spray) provides good results. Of course for *in vivo* applications, the paint should be chosen not to alter the tissue; for instance make-up (mascara) has been shown to be a good candidate (Jacquemoud *et al* 2007).

At last, some of the authors applied the method on the transmitted intensity pattern through a transparent medium, within a single cell using conventional optic of a microscope. Optical micro-elastography was conducted at a scale never reached up to now (Sandrin *et al* 2002). It thus fully validates the interest of digital image correlation for wave detection and tissue characterization.

5. Conclusion

We propose in this work an optical elastography method based on digital image correlation of white light speckle intensity. This approach is shown to efficiently track surface Rayleigh waves on soft tissues to further estimate their speed. In the present manuscript, a systematic study of the variability fully validates the reliability of measurements. Accurate estimations of surface wave speed were provided on isotropic, anisotropic and non-

plane soft tissues. The final aim of this approach is surface elasticity imaging. Natural surface waves in living tissue could be used to extract the mechanical parameter. Such a non-contact passive elastography method could be benefit for mechanical characterization of cornea (e.g. using an air puff (Wang *et al* 2012)) or of skin. Deducing the tissue stiffness from shear wave speed measurements is usually performed in the core of the tissue. However, one can imagine using the proposed method for subsurface phenomena, such as epidermis characterization in healthy and cancerous cases. Possible application using endoscopic camera can also be envisioned.

Acknowledgment

This work was partly funded by ANSYS France. We deeply thank LBMC UMR_T9406 for lending us the two Photron cameras. We acknowledge ARC 2018 of PhysiCancer and France Life Imaging FLI (WP3-FLI).

References

Athanasiou A *et al* 2010 Breast lesions: quantitative elastography with supersonic shear imaging—preliminary results *Radiology* **256** 297–303

Bel-Brunon A, Kehl S, Martin C, Uhlig S and Wall W A 2014 Numerical identification method for the non-linear viscoelastic compressible behavior of soft tissue using uniaxial tensile tests and image registration—application to rat lung parenchyma *J. Mech. Behav. Biomed. Mater.* **29** 360–74

Bercoff J, Tanter M and Fink M 2004 Supersonic shear imaging: a new technique for soft tissue elasticity mapping *IEEE Trans. Ultrason. Ferroelectr. Freq. Control* **51** 396–409

Boyce B L, Grazier J M, Jones R E and Nguyen T D 2008 Full-field deformation of bovine cornea under constrained inflation conditions *Biomaterials* **29** 3896–904

Brunon A, Bruyere-Garnier K and Coret M 2010 Mechanical characterization of liver capsule through uniaxial quasi-static tensile tests until failure *J. Biomech.* **43** 2221–7

Catheline S, Thomas J-L, Wu F and Fink M A 1999 Diffraction field of a low frequency vibrator in soft tissues using transient elastography *IEEE Trans. Ultrason. Ferroelectr. Freq. Control* **46** 1013–9

Chatelin S *et al* 2014 Anisotropic polyvinyl alcohol hydrogel phantom for shear wave elastography in fibrous biological soft tissue: a multimodality characterization *Phys. Med. Biol.* **59** 6923

Gao Z and Desai J P 2010 Estimating zero-strain states of very soft tissue under gravity loading using digital image correlation *Med. Image Anal.* **14** 126–37

Grasland-Mongrain P *et al* 2018 Ultrafast imaging of cell elasticity with optical microelastography *Proc. Natl Acad. Sci.* **115** 861–6

Jacquemoud C, Bruyere-Garnier K and Coret M 2007 Methodology to determine failure characteristics of planar soft tissues using a dynamic tensile test *J. Biomech.* **40** 468–75

Jones I 2018 A good practices guide for digital image correlation *International Digital Image Correlation Society*

Li S, Mohan K D, Sanders W W and Oldenburg A L 2011 Toward soft-tissue elastography using digital holography to monitor surface acoustic waves *J. Biomed. Opt.* **16** 116005

Liu C-H *et al* 2017 Ultra-fast line-field low coherence holographic elastography using spatial phase shifting *Biomed. Opt. Express* **8** 993–1004

Moerman K M, Holt C A, Evans S L and Simms C K 2009 Digital image correlation and finite element modelling as a method to determine mechanical properties of human soft tissue *in vivo J. Biomech.* **42** 1150–3

Nahas A, Tanter M, Nguyen T-M, Chassot J-M, Fink M and Boccara A C 2013 From supersonic shear wave imaging to full-field optical coherence shear wave elastography *J. Biomed. Opt.* **18** 121514

Nightingale K, Soo M S, Nightingale R and Trahey G 2002 Acoustic radiation force impulse imaging: *in vivo* demonstration of clinical feasibility *Ultrasound Med. Biol.* **28** 227–35

Royer D and Dieulesaint E 2000 *Elastic Waves in Solids I: Free and Guided Propagation* (Berlin: Springer)

Sandrin L *et al* 2003 Transient elastography: a new noninvasive method for assessment of hepatic fibrosis *Ultrasound Med. Biol.* **29** 1705–13

Sandrin L, Catheline S, Tanter M, Hennequin X and Fink M 1999 Time-resolved pulsed elastography with ultrafast ultrasonic imaging *Ultrason. Imaging* **21** 259–72

Sandrin L, Tanter M, Gennisson J L, Catheline S and Fink M 2002 Shear elasticity probe for soft tissues with 1-D transient elastography *IEEE Trans. Ultrason. Ferroelectr. Freq. Control* **49** 436–46

Sarvazyan A P, Rudenko O V, Swanson S D, Fowlkes J B and Emelianov S Y 1998 Shear wave elasticity imaging: a new ultrasonic technology of medical diagnostics *Ultrasound Med. Biol.* **24** 1419–35

Sporea I *et al* 2013 Acoustic radiation force impulse and supersonic shear imaging versus transient elastography for liver fibrosis assessment *Ultrasound Med. Biol.* **39** 1933–41

Sugimoto T, Ueha S and Itoh K 1990 Tissue hardness measurement using the radiation force of focused ultrasound *IEEE Ultrasonics on Symp., Proc.., 1990* pp 1377–80

Sutton M A, Orteu J J and Schreier H 2009 *Image Correlation for Shape, Motion and Deformation Measurements: Basic Concepts, Theory and Applications* (Berlin: Springer)

Walker W F and Trahey G E 1994 A fundamental limit on the accuracy of speckle signal alignment *1994 Proc. of IEEE Ultrasonics Symp.* vol 3, pp 1787–91

Wang S and Larin K V 2014 Shear wave imaging optical coherence tomography (SWI-OCT) for ocular tissue biomechanics *Opt. Lett.* **39** 41–4

Wang S *et al* 2012 Noncontact measurement of elasticity for the detection of soft-tissue tumors using phase-sensitive optical coherence tomography combined with a focused air-puff system *Opt. Lett.* **37** 5184–6

Zhang X and Greenleaf J F 2007 Estimation of tissue's elasticity with surface wave speed *J. Acoust. Soc. Am.* **122** 2522–5

Zorgani A *et al* 2015 Brain palpation from physiological vibrations using MRI *Proc. Natl Acad. Sci.* **112** 12917–21